Editors' Suggestion

# Design study of a high-brightness high-repetition rate thermionic injector for free-electron laser application: The architecture

Vitaliy Goryashko,[1,2,*] Kazuaki Togawa,[1,†] Peter Salén,[2] and Anatoliy Opanasenko[2,1]

[1]*RIKEN SPring-8 Center, Hyogo 679-5148, Japan*

[2]*FREIA Laboratory, Department of Physics and Astronomy, Uppsala University, Ångströmlaboratoriet, 75120, Uppsala, Sweden*

(Received 16 March 2025; accepted 28 July 2025; published 11 September 2025)

SACLA is the world's most compact hard x-ray free-electron laser and has been successfully and reliably operated for over a decade. To meet increasing user demands, an upgrade of the SACLA linear accelerator is planned in order to achieve a kHz-level repetition rate and enhanced beam brightness. A key component of this upgrade is a new injector, based on the existing pulsed dc gun with a thermionic cathode, which has demonstrated high beam quality, excellent stability, and simple maintenance. In this work, we present an in-depth beam dynamics study of a highly promising new SACLA injector architecture. Multistage velocity bunching, combined with one stage of magnetic compression and careful control of emittance growth, allows for up to 3 orders of magnitude of bunch compression while keeping the emittance growth at the submicron level. Our optimization approach utilizes a genetic algorithm coupled to 3D space-charge-dominated beam tracking to refine beam performance and identify optimal injector parameters. Thus, we demonstrate that the proposed injector can deliver electron beams with bunch durations and emittances comparable to those produced by the state-of-the-art *C*-band injector based on an rf photocathode gun [A. Giribono *et al.*, Phys. Rev. Accel. Beams **26**, 083402 (2023)]. Additionally, our extensive beam dynamics analysis of the dc electron gun (see part 2) provides valuable insights applicable to low-voltage continuous-wave very high frequency guns and superconducting radio-frequency guns.

DOI: 10.1103/b7sd-jvxq

## I. INTRODUCTION

The first generation of x-ray free-electron lasers (XFELs), LCLS [1] and SACLA [2], unleashed a transformational wave of time-resolved studies of how atoms and molecules move on their natural timescales. The *peak brightness* of XFELs exceeded that of synchrotrons by 10 orders of magnitude and enabled biological imaging with femtosecond x-ray pulses [3]. X-ray FELs are now a key instrument for studying atomic and molecular processes, condensed matter states, matter under extreme conditions, and chemical and biological reactions at the fundamental level [4,5].

The success of the first XFELs triggered the construction of new XFEL facilities (PAL [6], SwissFEL [7], and European XFEL [8]). In quest of higher *average brightness*, the repetition rate of XFEL pulses has been increased to the MHz level by using superconducting accelerators (LCLS-II [9] and SHINE [10]). To match increasing user demands, the SACLA XFEL is planned to be upgraded to the kHz repetition rate level [11,12]. We report on possible upgrade scenarios and a potential new injector architecture.

The present SACLA injector is based on a pulsed dc thermionic gun, which produces microsecond-long electron bunches with a submicron-level emittance [13–15]. A nanosecond bunch is extracted from the long electron pulse by means of a high-voltage chopper [16]. The gun has been in operation for 20 years, demonstrating high reliability, stability, simple maintenance, and the high quality of the electron beam [17]. Leveraging on this success, the upgraded injector will also utilize a pulsed dc thermionic gun. There is, however, a caveat: the ns electron bunch must be compressed down to the 10-fs level for many FEL applications. Therefore, the compression scheme in the present SACLA accelerator [18,19] is more complex than that, for example, of LCLS-I [20,21].

In the design of a new injector proposed for the SACLA high-repetition-rate upgrade, a great deal of efforts was devoted to developing a stable and tunable compression architecture capable of delivering electron beams with parameters competitive with those of the newest generation of linear accelerators for XFELs. In particular, we demonstrate that the proposed injector delivers 500 pC bunches

*Contact author: vitaliy.goryashko@physics.uu.se, vitgor06@gmail.com

†Contact author: togawa@spring8.or.jp

*Published by the American Physical Society under the terms of the Creative Commons Attribution 4.0 International license. Further distribution of this work must maintain attribution to the author(s) and the published article's title, journal citation, and DOI.*

with the duration and emittance comparable to those of the *C*-band injector based on a photogun technology designed at INFN [22].

## II. OVERVIEW OF THE LOW-ENERGY PART OF THE INJECTOR

In this section, we give a brief overview of the complete injector and explain the physics-based considerations that led us to a specific injector architecture. In order to increase the repetition rate of the SACLA XFEL from the current 60 Hz operation to 600 Hz operation [12], a new accelerator based on *X*-band technology [23] is planned. The high frequency of the *X*-band accelerating field places a more strict requirement on the maximum bunch duration such that the bunch can efficiently be captured and accelerated. We aim at picosecond (ps) bunch duration at the low-energy end of the injector and at sub-ps bunch duration at the high-energy end of the injector, which also includes a magnetic bunch compressor. The present study is mostly focused on the *low-energy part of the injector*, having the final beam energy of around 50 MeV. A tentative study of magnetic compression at around 120 MeV is also included for completeness.

### A. The concept

Figure 1 schematically shows the concept of the injector under study while Fig. 2 provides details on the field distributions and evolution of the beam parameters. The injector can be effectively divided into 8 regions (marked I–VIII in Fig. 2): (i) Region 1: generation of a few-μs electron beam in a pulsed 500-kV dc gun and correction of the beam divergence by a magnetic lens; (ii) Region 2: extraction of a 500-ps electron bunch by means of a high-voltage chopper and mild transverse focusing into a 238-MHz rf buncher for imprinting an energy-position correlation (energy chirp); (iii) Region 3: ballistic bunching in free space via a shear motion of the bunch distribution in the longitudinal phase space caused by the previously imprinted energy chirp. (iv) Region 4: bunch injection into a three-cell cavity and half-wavelength bunching (HWB) [24]. Note the rapid decrease in the bunch duration and the dip in the energy gain profile; (v) Region 5: velocity bunching [25,26] and acceleration in the remaining part of the three-cell cavity; (vi) Region 6: emittance compensation by the field of a magnetic lens [27]; (vii) Region 7: velocity bunching and acceleration in a traveling-wave *S*-band structure with simultaneous emittance compensation by a long solenoid [28]; (viii) Region 8: continued acceleration and emittance compensation in the *S*-band structure in the regime of adiabatic invariant [29].

### B. Multistage bunching

The new injector architecture makes use of three stages of longitudinal bunch compression: (i) conventional ballistic bunching, (ii) half-wavelength bunching (HWB), and (iii) conventional velocity bunching [25,26]. The second method of compression was discovered very recently [24] and deserves further explanation. The process of HWB is illustrated in Fig. 3. In the conventional velocity bunching scheme, a low-energy bunch is injected at the zero crossing of the accelerating field, and if the accelerating gradient is chosen correctly, the injected bunch moves up to the crest. The bunch is also longitudinally compressed, which is caused by velocity modulation, as the head particles experience a lower accelerating field than the tail particles [30].

At the same time, the experiment [28] showed that even stronger compression can be achieved if the bunch is

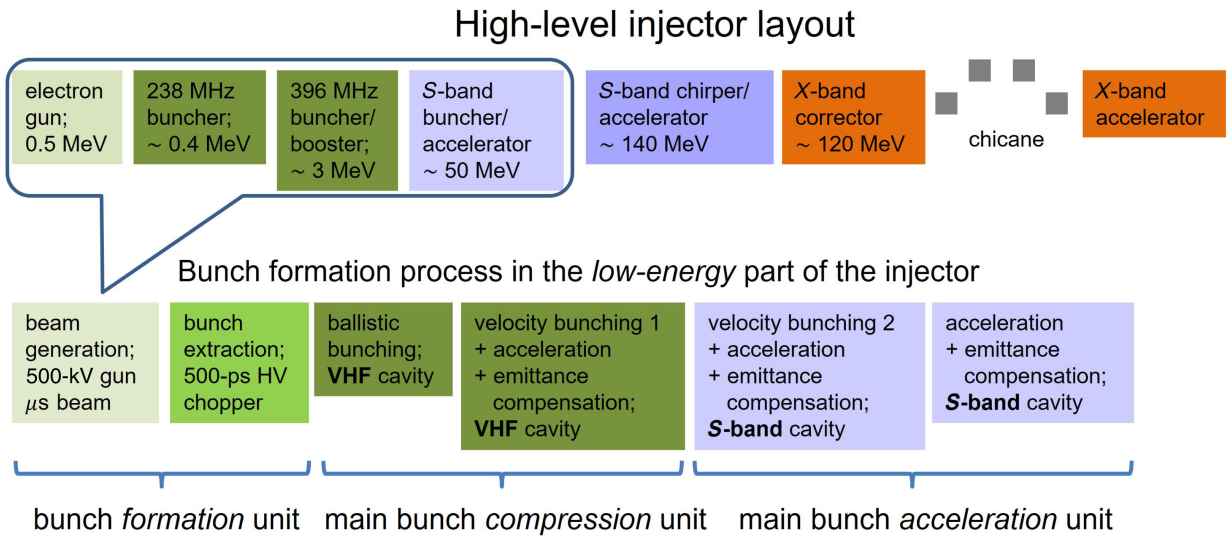



FIG. 1. A high-level conceptual layout of the new injector.

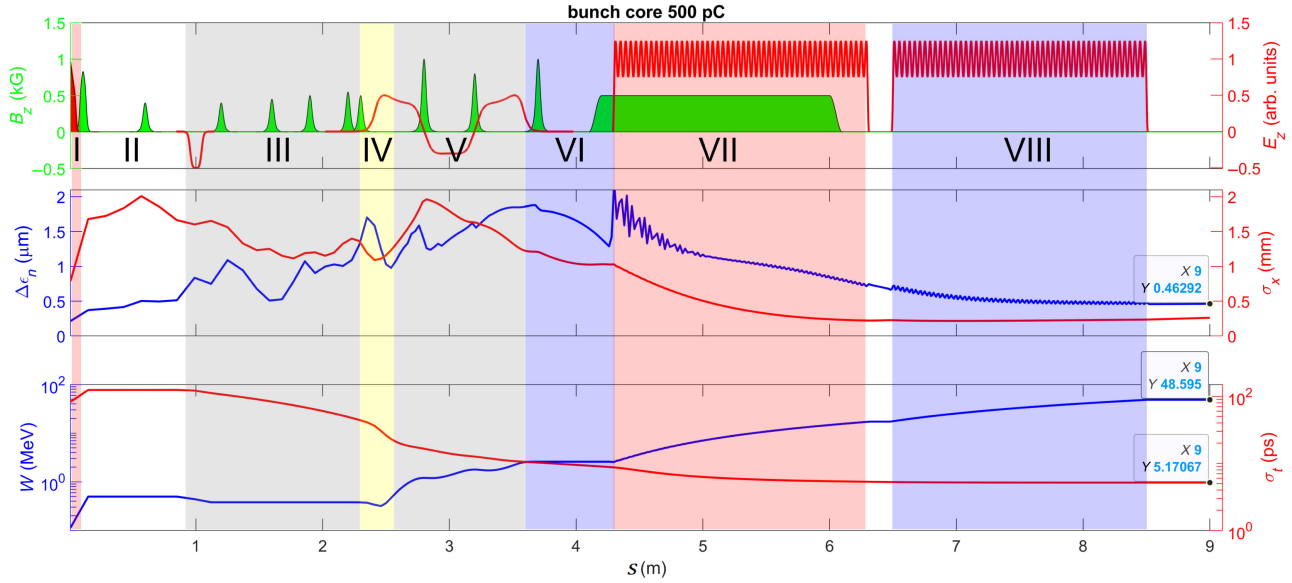



FIG. 2. Evolution of beam parameters in the low-energy part of the injector. Top plot: longitudinal distributions of the static magnetic fields (green filled areas) and rf fields (red lines). Middle plot: evolution of the projected emittance growth (blue) and rms beam size (red) along the injector. Bottom plot: evolution of the bunch energy (blue) and rms duration (red) along the injector.

injected earlier than the zero crossing of the accelerating field. This idea was further developed in [24], and it turned out that strong compression can be achieved on the scale of the half-wavelength in the first cell of an accelerating structure if the bunch is injected into a deeply decelerating phase. When the phase and the gradient upon injection are correctly chosen, the bunch first rapidly decelerates and acquires a large energy chirp, then rotates in the longitudinal phase space (compression), slips to the accelerating field, and recovers its energy. This process is illustrated in Fig. 3, where the longitudinal beam distribution is shown at multiple consecutive instances of time. What is also very important is that the bunch acquires a positive second-order energy chirp in the longitudinal phase space at the cavity entrance, which leads to the linearization of the phase space during the subsequent velocity bunching. Thus, making the overall compression very efficient, and the total compression factor in a multicell cavity can reach over 100 [24]. At the same time, the phase acceptance in this scenario is rather small, and in the present injector design, moderate compression is applied because of the very long bunch duration.

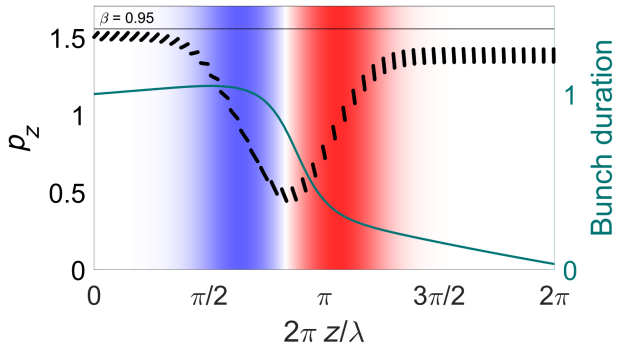



FIG. 3. An example of HWB in a single-cell cavity. The shaded red and blue regions represent the instantaneous electric field in the cavity acting on the electrons (short black lines represent the longitudinal bunch distribution). The bunch is injected into the decelerating phase (blue) but slips into the accelerating phase (red). The green line shows the ratio of the current bunch length to the initial one. Adapted from Ref. [24].

### C. Beam phase space

The resulting phase-space distributions of the bunch at the end of the injector are depicted in Fig. 4. One can draw several conclusions: (i) slices are well aligned in the transverse phase space; (ii) emittance oscillations are completely damped; (iii) the slice emittance *growth* is below 0.3 μm (the cathode thermal emittance is 0.4 μm); (iv) the bunch distribution is quite uniform; and (v) no overbunching in the longitudinal phase space.

We have considered several types of accelerating cavities to be used for HWB and acceleration. The spoke cavity is found to be the most advantageous in terms of the beam quality. This cavity allows for efficient local control of the transverse phase space of the beam by placing small solenoids at the ends of the cavity and inside the spokes. The latter might be technologically challenging but offers a great advantage by enabling a local correction of rf and space-charge defocusing effects. Alternative solutions include using other types of cavities with a quasiflat accelerating field profile, such as the booster cavity for

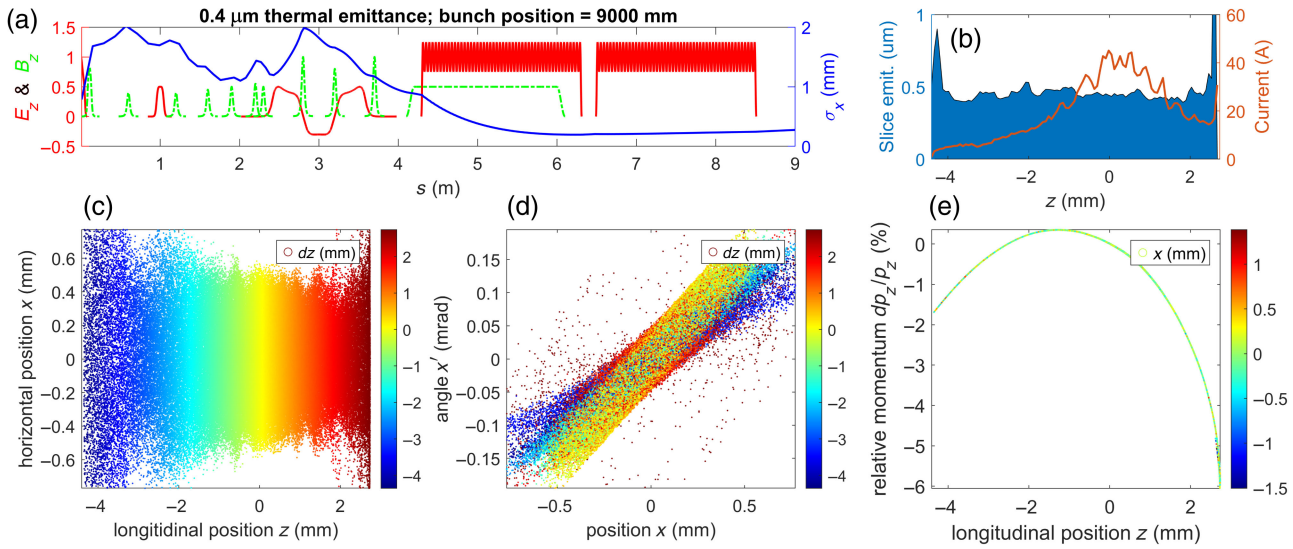



FIG. 4. Panel (a): the distributions of the static magnetic fields (green) and rf fields (red), and the evolution of the rms beam size (blue) along the injector. Panel (b): slice emittances (left axis) and current (right axis) along the bunch. Panel (c): the distribution of particles in the $xz$ plane. Panel (d): transverse phase space of the beam. Panel (e): longitudinal phase space of the beam.

SPring-8, used until 2021 before the direct beam injection from SACLA linac [31], and to place a solenoid around the cavity.

Note that the small modulation of the current present in Fig. 4 is an artifact of simulations, and when the number of particles in simulations is increased to $10^6$, this modulation disappears almost completely. However, the simulation of the whole injector with $10^6$ particles is challenging because of computational limitations. The artifact stems from the fact that the calculation of the bunch space-charge field is based on the representation of the bunch density distribution by a series of rings in order to take into account the image charge on the cathode.

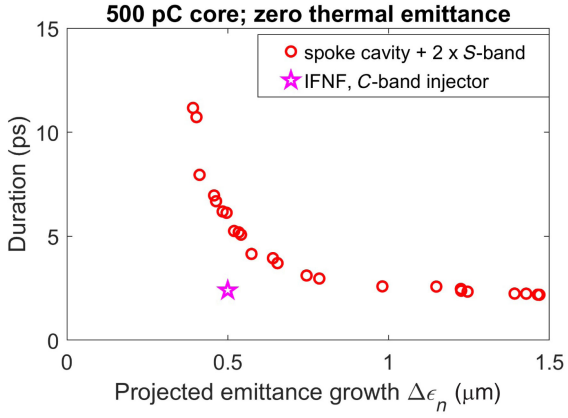



FIG. 5. Pareto frontier of the minimum possible emittance growth and rms bunch duration. The results are based on beam dynamics simulations controlled by a genetic optimization algorithm. For reference, the simulation result for the $C$-band INFN is also presented.

### D. Results of genetic optimization

Finally, we run a genetic optimization algorithm to determine the optimum injector parameters that result in the minimum emittance growth and bunch duration. A built-in MATLAB genetic optimizer was used to run ASTRA [32] simulations with $2 \times 10^4$ particles. The resulting Pareto frontier is depicted in Fig. 5. It turned out that tuning of the bunch emittance and duration is mostly achieved by changing the phases of the buncher, spoke-based booster, and the first $S$-band cavity. The magnetic field values change in a very narrow range. The rms bunch duration of 5 ps can be achieved with the growth of projected emittance of just 0.5 μm. Thus, our injector architecture allows for the production of 500-pC bunches with the parameters, see Table I, competitive to that of the $C$-band injector designed at INFN.

The achieved short bunch duration allows for further acceleration in an $X$-band linac preceded by one stage of magnetic compression in a chicane after the short $S$-band linac, see Fig. 1. Preliminary results on magnetic compression and phase-space linearization are presented in the

TABLE I. Representative set of beam parameters at the exit of different parts of the injector. Thermal emittance is 0.4 μm.

| Parameter | Gun | Spoke | Low-energy $S$-band | Chicane |
|---|---|---|---|---|
| Charge (nC) | 0.5 | 0.5 | 0.5 | 0.24 |
| Energy (MeV) | 0.5 | 2.8 | 48 | 124 |
| Projected emittance (μm) | 0.52 | 0.84 | 0.61 | 0.57 |
| rms duration (ps) | 125 | 14 | 5.2 | 0.2 |
| Peak current (A) | 1 | 25 | 45 | 480 |

last section, meanwhile, we proceed to the details of low-energy bunching.

## III. LOW-ENERGY BUNCHING IN A VHF CAVITY

After the HV chopper, the bunch is 500 ps and still too long for velocity bunching, therefore the original SACLA ballistic bunching section is left in place. It makes use of a 238-MHz single-cell standing wave cavity. Previous studies and the current one showed that it is advantageous to operate at around −120° with respect to the phase of the maximum energy gain. At this injection phase, the longitudinal phase space becomes a little bit concave, which allows for more uniform bunching as the bunch drifts in free space. The beam energy is simultaneously reduced to around 0.4 MeV, which makes the longitudinal focus shorter. However, because of the space-charge effect, the emittance starts to grow considerably before full bunching is achieved. Only moderate compression by a factor of 4–5 can be applied without additional mitigation measures.

*Our design philosophy is to minimize the growth of slice emittance* because it is irreversible. Hence, 1.5 m downstream the buncher cavity, the beam is injected into a booster that simultaneously accelerates and longitudinally compresses the beam. An example of the evolution of the mean slice emittance along the first 4.5 m of the injector is shown in Fig. 6. In order to make the result more pronounced, the *emittance growth* is shown instead of the total slice emittance. The latter also includes uncorrelated thermal emittance.

From Fig. 6, one can see that there is emittance growth to the level of approximately 0.15 μm after passing the first solenoid because of the aberrations *discussed in the part 2 of this design study*. Ballistic bunching is mild, and by tuning the focusing solenoids, the slice emittance is preserved—and even slightly reduced—up to the entrance of the spoke cavity. In the cavity, the slice emittance increases due to space-charge and rf effects, since, for example, rf defocusing is phase dependent and, in case of long bunches, cannot be completely compensated by static magnetic fields. The final

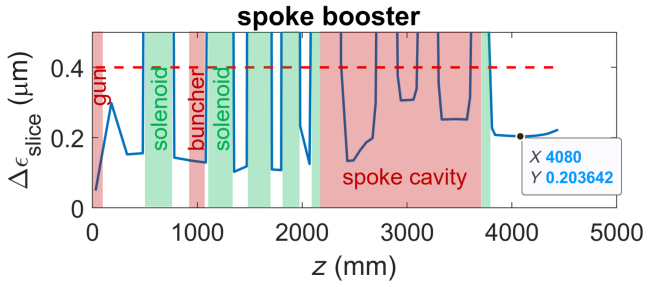



FIG. 6. Evolution of the mean slice emittance growth of the bunch. The red shaded areas depict the regions of rf or dc electric fields whereas the green shaded area depicts the regions where static magnetic fields are present. The thermal emittance level (red dashed line) is shown for reference.

mean slice emittance is 0.2 μm and still considerably smaller than the initial thermal emittance, whose level is represented by the red dashed line in Fig. 6.

### A. Choice of the VHF cavity

We have considered several cavity candidates for the booster, and the optimum solution is the spoke cavity. This cavity geometry was developed at ANL (U.S.) in the late 1980s by Delayen [33] for the acceleration of high-current medium velocity particles. It is used in modern superconducting accelerators ESS (Sweden) [34] and MYRRHA (Belgium) [35]. This cavity was designed for operation in a superconducting state at 4 K and its usage in a normal conducting accelerator is very unusual. However, nothing precludes operating this cavity at room temperature, since it provides a good shunt impedance of around 20 MΩ. In our case, it offers a significant advantage over other cavity geometries in terms of beam quality. Namely, the hollow structure of the spoke allows for the installation of a small solenoid for local correction of rf defocusing. Furthermore, it has a large velocity acceptance of over 95% in our case and a quite flat profile of the accelerating field. Other advantages include strong cell-to-cell coupling in a multi-spoke cavity and compactness: it is about half the size of a TM cavity of the same frequency [36]. At the same time, the spoke geometry also has a disadvantage: the electromagnetic eigenmode exhibits quadrupole components. By optimizing the spoke geometry, the impact of the quadrupole field components on the beam dynamics can be minimized [37].

### B. Genetic optimization of beam parameters

We used a genetic optimization algorithm built into MATLAB to run beam dynamics simulations in ASTRA and applied the optimization procedure to three accelerator architectures: (i) the present SACLA injector, which includes the part from the gun to the exit of the first *L*-band accelerating cavity; (ii) the same SACLA injector layout but with a new hybrid magnet, and (iii) finally, a compact injector layout—from the gun till the exit of the spoke cavity—introduced in Sec. II A. The resulting Pareto frontiers for the three architectures are shown in Fig. 7. For reference, the parameters of the INFN *C*-band injector operating with a 500 pC charge and no compression are also presented. First, we note that just by using a novel magnet design (*see part 2 of this design study*), the performance of the SACLA injector can be significantly improved in terms of emittance in the regime of moderate compression. We want to emphasize that the results for the projected emittance *growth* are presented. Thus, the total projected emittance will be different depending on the initial thermal emittance, which is mostly dictated by the cathode radius and operation temperature. In the simulation, the thermal emittance is set to zero, and the cathode radius is 1.5 mm. Such a simulation scenario

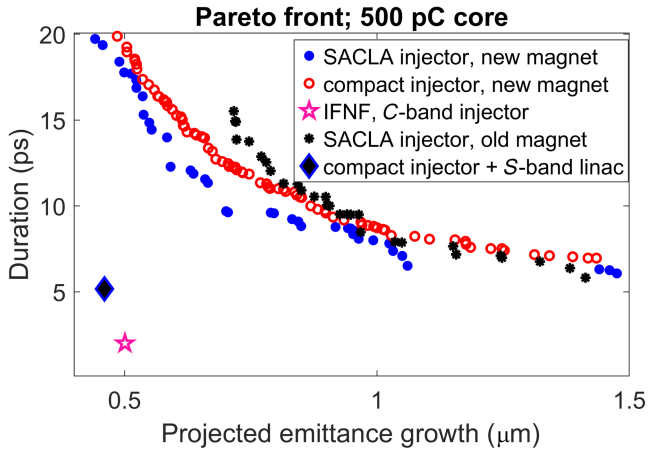



FIG. 7. Computed Pareto frontier of the rms bunch duration vs emittance growth for three injector architectures: the present SACLA injector (black asterisks); the same SACLA injector with a new hybrid magnet (blue dots), and the compact spoke-based injector (red circles). The INFN parameters are depicted by the purple star, and the compact injector complemented with a short *S*-band linac represented by the black diamond.

makes even subtle differences very clear and allows for more straightforward comparison between different regimes, see Table II.

Two stages of bunching, comprising ballistic and HWB, allow for compression by a factor of 10 with a moderate emittance growth of around 0.7 μm The compression by a factor of 20 is also possible but at the expense of a large emittance growth of 2.0 μm. The latter is caused by several factors: (i) overbunching of slices misaligned in the phase space, (ii) considerable deformation of the transverse phase caused by a strong space-charge force, and (iii) increased energy spread [38–40]. In the next section, we will discuss how the bunch can be compressed further without emittance growth using standard velocity bunching. Meanwhile, in Fig. 7, we also added one data point corresponding to our scenario with an additional short *S*-band linac. One can see that our final result—with the total compression factor of 25—is comparable to that of the simulated INFN *C*-band linac.

Figure 8 shows a set of spoke-based injector parameters corresponding to the Pareto frontier. The vertical scale represents different runs of the genetic optimization algorithm. The emittance and bunch duration resulting from runs with different injector parameters (green for magnetic field parameters and red for rf parameters) are shown in blue.

To extract *correlations between the injector parameters* and the resulting emittance growth and bunch duration, it is advantageous to represent the parameters in the form of relative deviations from the corresponding mean values. This is done in Fig. 9. One can see a very clear *correlation* between the change in emittance growth and bunch duration on the one hand and the change in the buncher field amplitude and booster phase on the other hand. This suggests that the whole injector can be tuned by a single knob, and we will demonstrate this below by tuning the phase of the spoke cavity field while keeping all other parameters constant.

The spoke-based injector is also quite immune to variations in the strength of focusing solenoids. This finding contrasts with that of the present SACLA injector. In the low-energy part of the present SACLA injector, four rf cavities are used, and the resulting beam parameters are sensitive to variations in solenoid field strength.

### C. Example of the evolution of beam parameters and phase space

Figure 10 shows the evolution of the rms beam parameters along the spoke-based injector. The projected emittance grows during bunching but then is compensated by a solenoid field after the spoke cavity. Note the more rapid bunch compression in the vicinity of the longitudinal position $s = 2.5$ m. The beam energy profile at this point exhibits a dip. This is the region of HWB.

Electron trajectories along the system are depicted in Fig. 11. In the injector, the bunch is adiabatically compressed longitudinally and transversely while being simultaneously accelerated.

The distribution of the rf and static magnetic field is depicted in panel (a) of Fig. 12. The peak current at the end of the injector reaches 25 A, panel (b), whereas the slice emittance is totally dominated by the initial thermal emittance of 0.4 μm. The phase-space distributions are plotted in panels (c)–(e). The core of the bunch has an *ellipsoidal shape* with a quite uniform density distribution, see panel (c) in Fig. 12. Therefore, *the resulting*

TABLE II. Normalized emittance $\varepsilon_n$ (μm) for three injector architectures and two compression regimes. The final beam energy, $W$, and the injector length, $L$, are different.

| Regime | Mild compression $\sigma_t = 15$ ps | | | Strong compression $\sigma_t = 7$ ps | | |
|---|---|---|---|---|---|---|
| Injector | SACLA old magnet | SACLA new magnet | Spoke cavity | SACLA old magnet | SACLA new magnet | Spoke cavity |
| $\Delta\varepsilon_n$ (μm) | 0.72 | 0.54 | 0.61 | 1.25 | 1.05 | 1.44 |
| $W$ (MeV) | 17.1 | | 2.7 | 16.4 | | 2.6 |
| $L$ (m) | 7.3 | | 4.5 | 7.3 | | 4.5 |

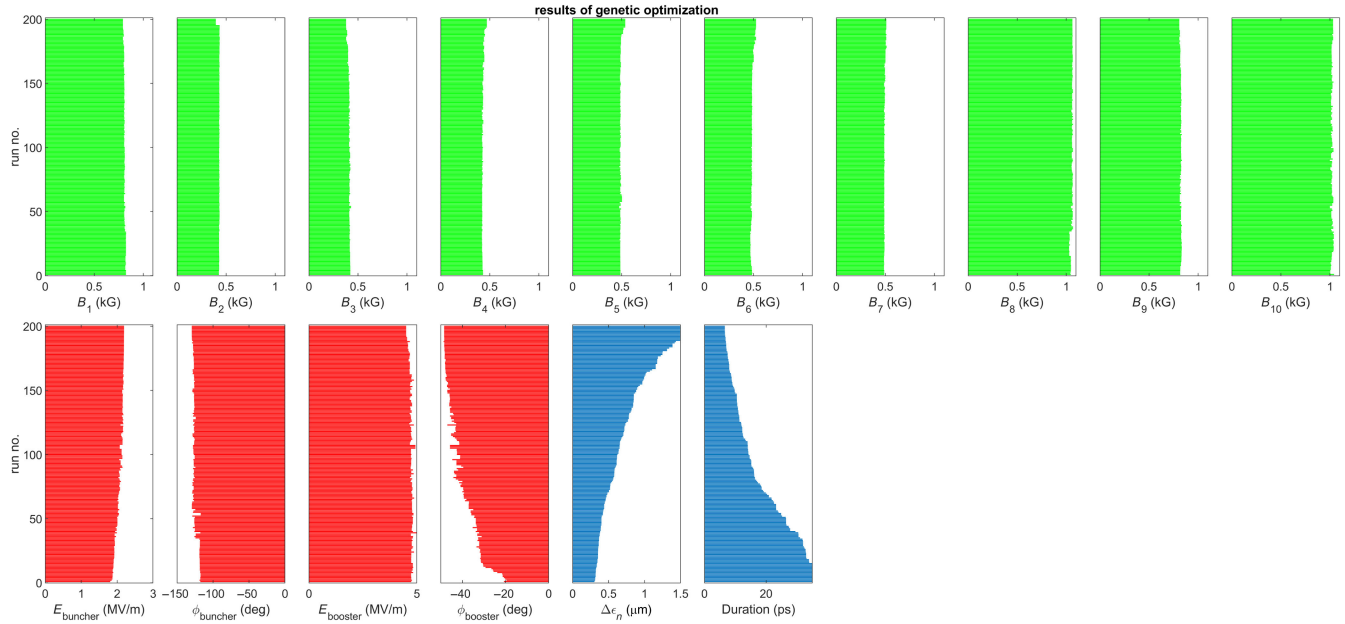



FIG. 8. Parameters of the injector components yielding the Pareto frontier shown in Fig. 7. The upper row gives the parameters of the magnetic lenses, the bottom row gives the parameters of the rf cavities (peak field and phase), as well as the resulting emittance growth and bunch duration.

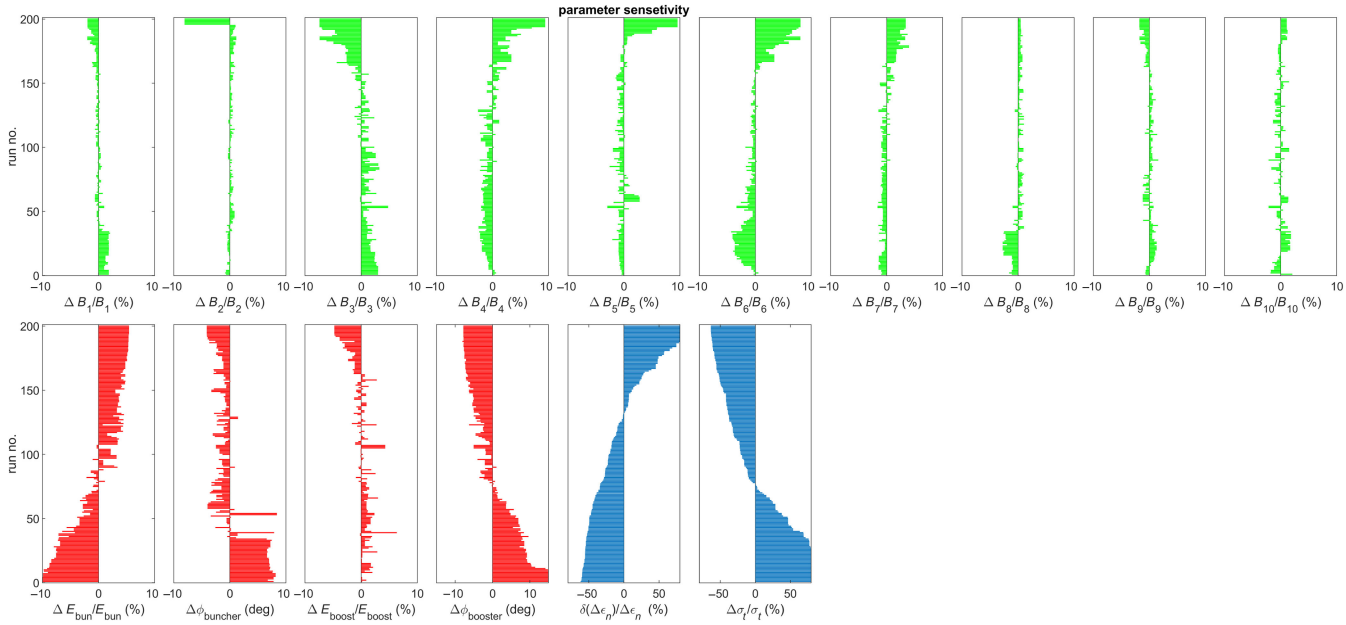



FIG. 9. The same set of parameters as in Fig. 8, but now, the relative deviation from the mean value is shown.

*space-charge force is linear in the bunch core*, which we have checked using the built-in ASTRA postprocessing.

The longitudinal positions of electrons are color coded, which allows one to distinguish different slices in the transverse phase space seen in panel (d) of Fig. 12. The head and tail slices are misaligned with respect to the core slices; otherwise, emittance compensation is almost complete.

### D. Half-wavelength bunching and emittance compensation

The results of genetic optimizations shown in Fig. 8 suggest that the optimum range of phases of the spoke cavity is from −50° to −20°. In this case, the beam is injected into a deeply decelerating phase of the spoke cavity, and the mechanism of HWB occurs, see Sec. II B.

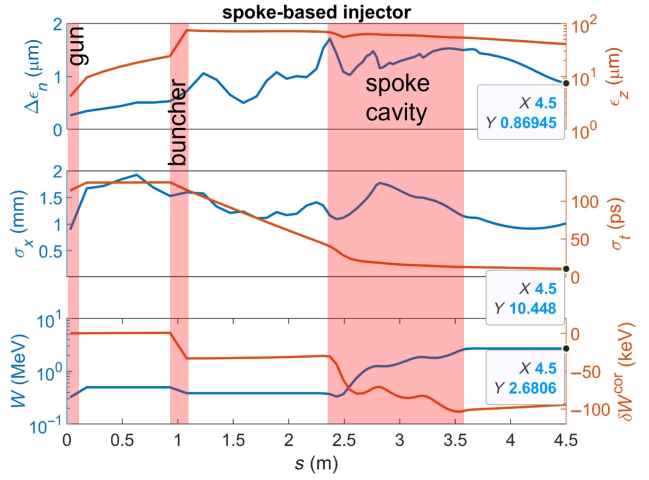



FIG. 10. Longitudinal evolution of the rms beam parameters. Upper plot: transverse emittance growth (left axis) and longitudinal emittance (right); Middle plot: rms beam size (left) and rms bunch duration (right); Bottom plot: mean beam energy (left) and rms correlated energy spread (right).

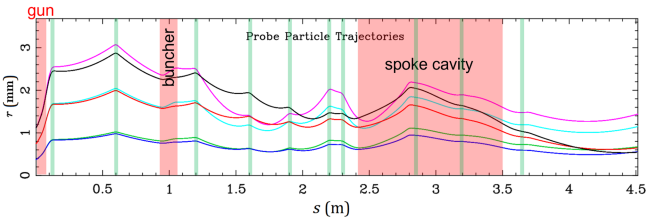



FIG. 11. Trajectories of electrons in the spoke-based injector.

To test the tunability of the injector, we run a scan of the spoke cavity phase while keeping all other parameters fixed. The variation of the beam parameters is shown in Fig. 13. More negative phases correspond to stronger HWB and less energy gain, whereas for less negative phases, HWB does not occur and the bunch is compressed only slightly via standard velocity bunching. As the phase is changed from −20° to −50°, the parametric dependence of the bunch duration on the emittance is formed as presented in Fig. 14. This finding is very important as it proves that the bunch duration can be tuned by a single knob—by the phase of the spoke cavity.

### E. Sensitivity study and alternative bunching booster configurations

In an experiment, we usually do not know exactly the value of each parameter or setting of an accelerator component. In addition, beam diagnostics is also limited, and the phase-space distribution is known only at a few locations along the accelerator. Hence, the question arises: "How well can we optimize the accelerator performance given limited information about the accelerator and beam parameters?" The results in Fig. 15 are an attempt to answer the above question. The starting point of the analysis is the optimum regime of the spoke cavity-based injector. This regime is represented by the green diamond. Then, we added a random uncorrelated spread of 1% to each parameter and performed 400 runs. Each run has its own random set of parameter variations. The result is a distribution of possible values of the emittance growth and bunch duration. We calculated the mean emittance

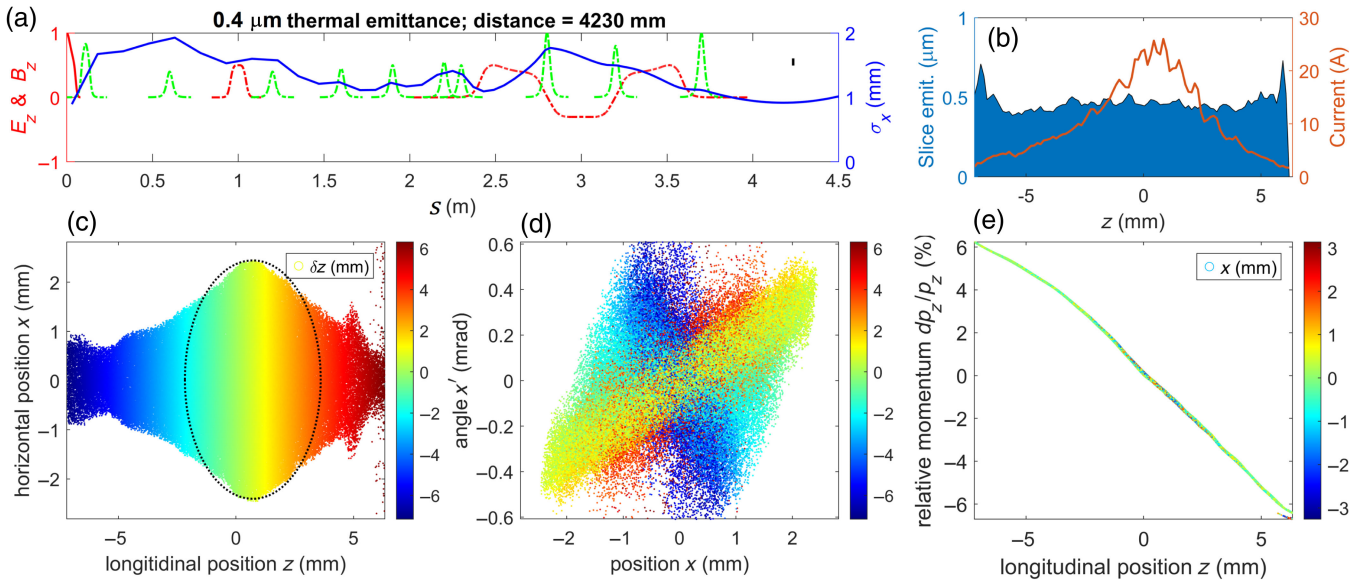



FIG. 12. Panel (a): the distributions of the static magnetic fields (green) and RF fields (red), and the evolution of the rms beam size (blue) along the injector. Panel (b): slice emittances (left axis) and current (right axis) along the bunch. Panel (c): the distribution of particles with the *elliptically shaped* core in the $xz$ plane. Panel (d): transverse phase space of the beam. Panel (e): longitudinal phase space of the beam.

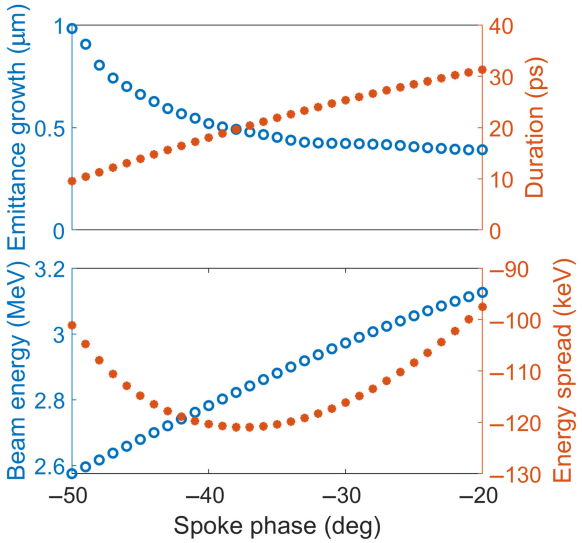



FIG. 13. Beam parameters vs the phase of the spoke cavity. Top plot: emittance (left axis) and bunch duration (right); Bottom plot: mean beam energy (MeV) and rms energy spread (keV).

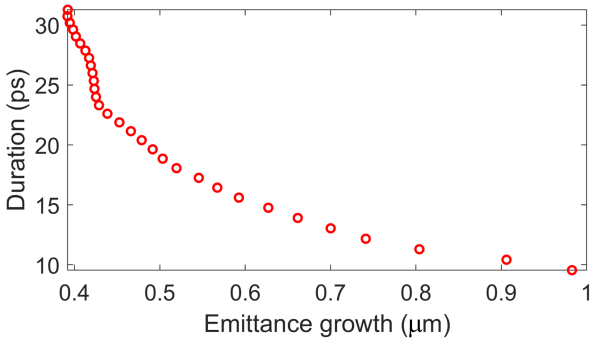



FIG. 14. Parameter tuning of the bunch duration as a function of the emittance growth when the spoke cavity phase is changed from −20° to −50°.

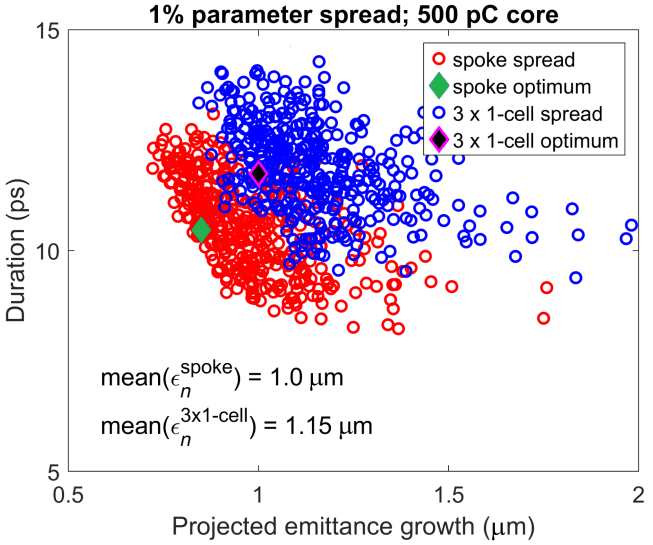



FIG. 15. Sensitivity of the bunch duration and emittance growth to a random parameter spread. The beam parameters corresponding to the optimum spoke-based injector and an injector based on three single-cell cavities are shown by the blue and black diamonds.

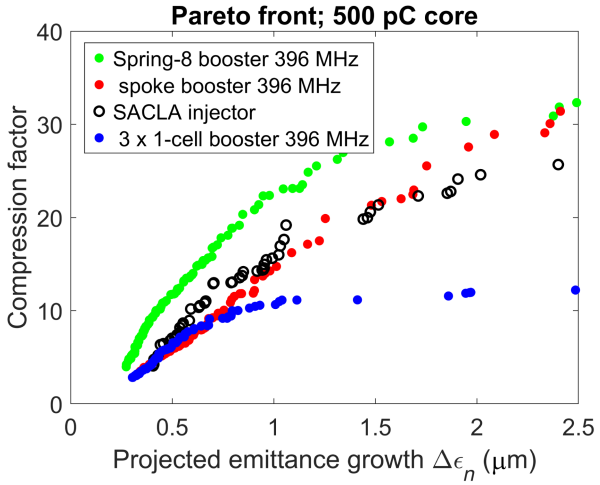



FIG. 16. Pareto frontier of the maximum compression and minimum emittance growth for four injector architectures: the present SACLA injector (black), the spoke-based injector (red), the injector based on three single-cell cavities (blue), and the injector based on a SPring-8 synchrotron booster cavity (green). The parameters are computed at $z = 4.5$ m, see Fig. 2.

growth, and it increased to 1.0 μm from the start value of 0.8 μm. It is interesting to note that the mean bunch duration changed negligibly. Thus, *any deviations from the optimum injector configuration result mostly in emittance growth*.

Technical realization of the spoke cavity with built-in small solenoids might be challenging; therefore, we considered an alternative configuration composed of three single-cell cavities with solenoids in between. The cavity is a scaled version of the SACLA 476-MHz booster cavity. The results of the sensitivity study to random variations of the parameters are also shown in Fig. 15. This alternative injector configuration shows a greater sensitivity to the parameter spread, and even the optimum configuration demonstrated worse performance.

In addition, yet another possible solution for the booster includes a SPring-8 booster cavity [31], whose EM design was adjusted in SUPERFISH and contains only three cells instead of the original five cells. Two large solenoids around the first and third cells of the cavity are assumed. The space around the second cell is kept free for connecting an rf coupler and vacuum pumps.

The optimum performance of four injector architectures, including the optimized present SACLA injector layout, is compared in Fig. 16. The spoke-based injector demonstrates good performance comparable to that of the SACLA injector while being much simpler than the original

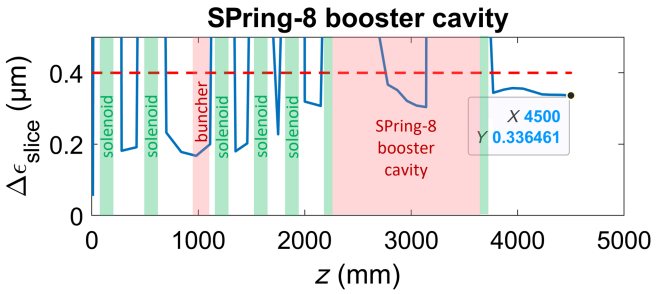



FIG. 17. Slice emittance growth along the SPring-8 booster cavity-based injector. The final bunch duration is the same as in Fig. 6 and equal to 10 ps rms.

SACLA design. The injector based on three single-cell cavities does not reach the same level of performance as the above two injectors. The configuration based on the SPring-8 booster cavity shows superior performance and is a potential candidate for the future upgrade. At the same time, compared to the spoke cavity-based solution, the slice emittance growth is 65% higher in the SPring-8 booster cavity-based injector (see Fig. 17). In what follows, we will consider magnetic compression for both cavity configurations as the most promising.

## IV. HIGHER-ENERGY BUNCHING IN AN *S*-BAND CAVITY

The INFN experiment [28] clearly showed that velocity bunching is compatible with emittance compensation and the oscillations of emittance can be damped while the beam is accelerated and compressed. Hence, we employ the same strategy and assume an *S*-band structure immersed into a focusing magnetic field of a long solenoid. Since the upgraded SACLA injector must run at 600 Hz, we limit the accelerating gradient to relatively low values in order to minimize rf heat load. The first *S*-band structure has a gradient of around 12 MV/m and the typical solenoid field in the design is 0.44 kG (44 mT).

### A. Velocity bunching and emittance compensation

Figure 18 shows a scan of the beam parameters as a function of the phase of the first *S*-band cavity. Zero phase is defined as the phase of the maximum energy gain. The maximum compression is achieved at −80° with the final bunch length being less than 1 mm. The emittance growth is, however, huge because of overbunching and mixing of slices with different orientations in the transverse phase space. This emittance growth is irreversible. Therefore, we apply only mild compression in order to avoid overbunching.

The results in Fig. 18 are presented for the magnetic field optimized for the phase of −60°, therefore the emittance attains the minimum at that phase. Genetic optimization, discussed below, showed the optimum range of phases is between −65° and −55°. The phase of the second *S*-band

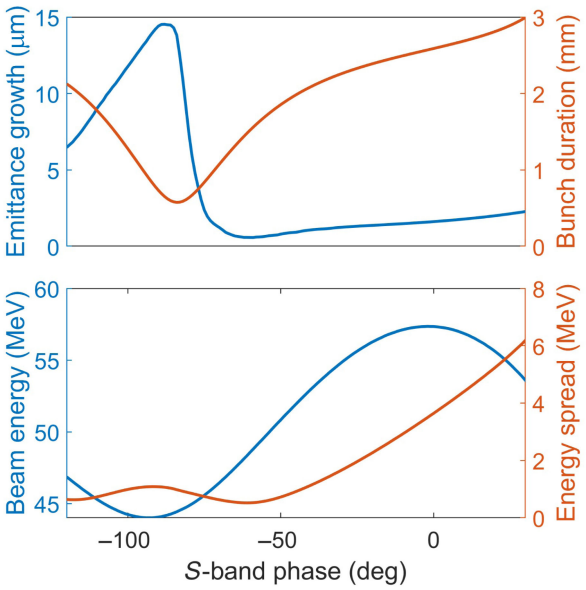



FIG. 18. Scan of the beam parameters vs the phase of the first *S*-band cavity. Top plot: projected emittance and bunch length. Bottom plot: mean beam energy and energy spread.

cavity is set to 30°—the optimum value found by the genetic algorithm.

Several snapshots of the $xz$ and $xx'$ beam distributions along the *S*-band section of the injector are presented in Fig. 19. The longitudinal bunch compression is moderate, but the very head of the electron distribution is overbunched because the bunch "sees" a decelerating phase in the first cell of the *S*-band structure. The overbunching locally creates a strong defocusing space-charge field and the electrons are pushed sideways forming a halo. A collimator might be needed after the second *S*-band structure.

### B. Comparison of different booster options

In Sec. III E, we found that the SPring-8 booster cavity provides superior compression of the bunch. However, once the *S*-band linac is added for emittance compensation and acceleration, the performance of the SPring-8 booster is less impressive and even worse than that of the spoke cavity booster, see Fig. 21. The latter allows for local correction of beam dynamics by means of built-in small solenoids and, as a result, smaller growth of the slice emittance, cf. Fig. 6 vs Fig. 17.

To understand the subtle difference in the slice emittance growth and the projected emittance between the spoke cavity-based and SPring-8 booster cavity-based injectors, we need to come back to the process of bunch compression and formation. In the case of the spoke cavity, velocity bunching occurs primarily in the region free from confining magnetic fields. The bunch is allowed to expand naturally and its divergence is corrected locally. Thanks to this unconfined expansion, the bunch distribution becomes

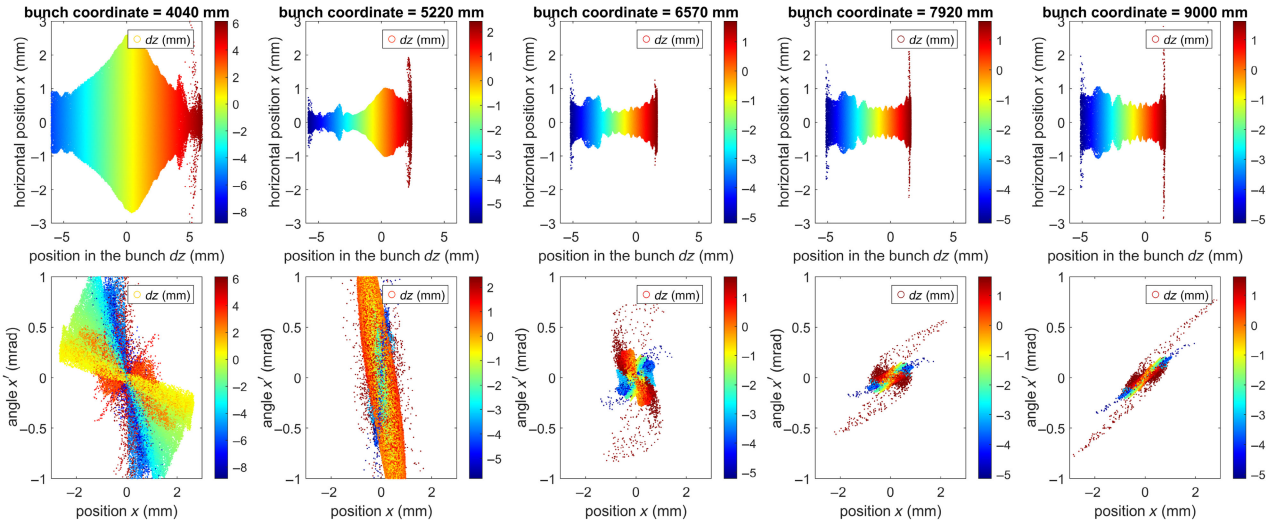



FIG. 19. Snapshots of the $xz$ beam distributions (top plots) and $xx'$ distributions (bottom plots) at different positions along the $S$-band section of the injector.

elliptically shaped as shown in Fig. 4(c). The particles are getting grouped in the middle of the bunch, increasing the local space charge and pushing outward the outer particles. The distributions of the radial space-charge field in different planes of the bunch are depicted in Fig. 20.

The situation with the bunch formation is different in the SPring-8 booster cavity because the correcting solenoids are located around the cavity. The longitudinal extent of the solenoid field is of the order of its diameter. The diameter of the 396 MHz SPring-8 booster cavity is approximately 500 mm so that even a short solenoid around the cavity will have the magnetic field extending over the distance of 500 mm. This implies that the electrons of the bunch are moving in a confining magnetic field during velocity bunching. The natural transverse expansion of the bunch is suppressed, and the resulting bunch distribution becomes egg like. The space-charge electric field has different strength in different cross sections as it is depicted in Fig. 20. The radial field distribution is also slightly nonlinear, which explains a higher slice emittance growth.

## V. TENTATIVE CONSIDERATIONS ON MAGNETIC COMPRESSION

In order to complete the design study of the new potential injector architecture, in this section, we present preliminary results of bunch compression in a magnetic compressor represented by a chicane. As depicted in Fig. 1, after the low-energy part of the injector, the beam is further accelerated by the $S$-band accelerator. The acceleration is accomplished off crest in order to imprint a negative position-energy correlation into the bunch for compression in the chicane. An $X$-band accelerator structure is added in order to correct for the nonlinear rf curvature induced by the $S$-band accelerating fields. Following the successful approach already implemented in the SACLA linac, the

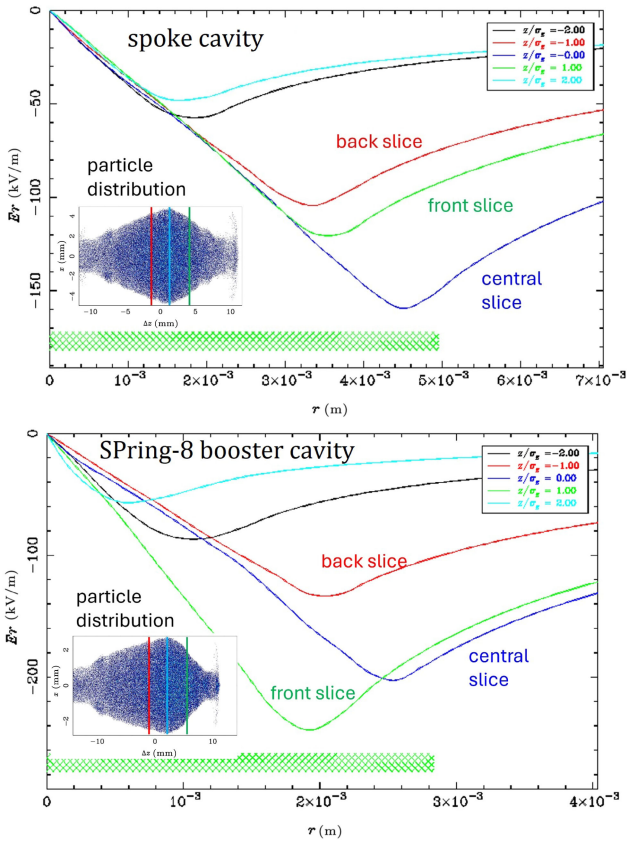



FIG. 20. Distributions of the radial space-charge field in different planes of the bunch at the end of the first cell of the spoke and SPring-8 booster cavities. The insets show the corresponding particle distributions. A *local correction of the beam divergence* is implemented in the spoke cavity by means of built-in small solenoids whereas the SPring-8 booster cavity is surrounded by two large solenoids providing *"global" correction of the beam divergence*. The green bar at the bottom of the plot indicates the bunch radius.

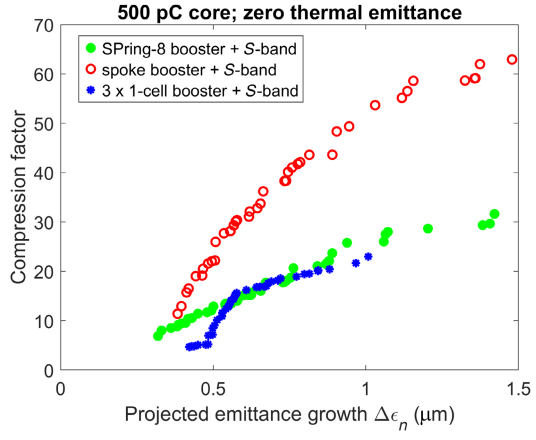



FIG. 21. Pareto frontier of the maximum compression and minimum emittance growth for three injector architectures: the spoke-based injector (red), the injector based on three single-cell cavities (blue), and the injector based on a SPring-8 synchrotron booster cavity (green). The parameters are computed at $z = 9$ m after the *S*-band linac, see Fig. 2.

longitudinal phase space is overcorrected in order to prepare the beam for compression in the subsequent chicane at a higher energy [19]. First, we will scan a broad parameter space within a 1D approximation and then perform more detailed space-charge dominated 3D simulations of the most interesting regimes.

### A. Wide parameter scan with LiTrack

To obtain an overview of achievable compression factors and resulting beam profiles, we performed 1D simulations using the code LiTrack developed at SLAC [41]. This code tracks 1D distributions of particles taking into account rf acceleration, wakefields in accelerating structures, and bunch compression up to the third order with respect to relative energy deviation.

The phase of the higher-energy *S*-band accelerator, bringing the beam to 140 MeV from 50 MeV, was scanned with LiTrack, and the resulting bunch current distribution, the mean slice energy, and slice energy spread along the bunch are

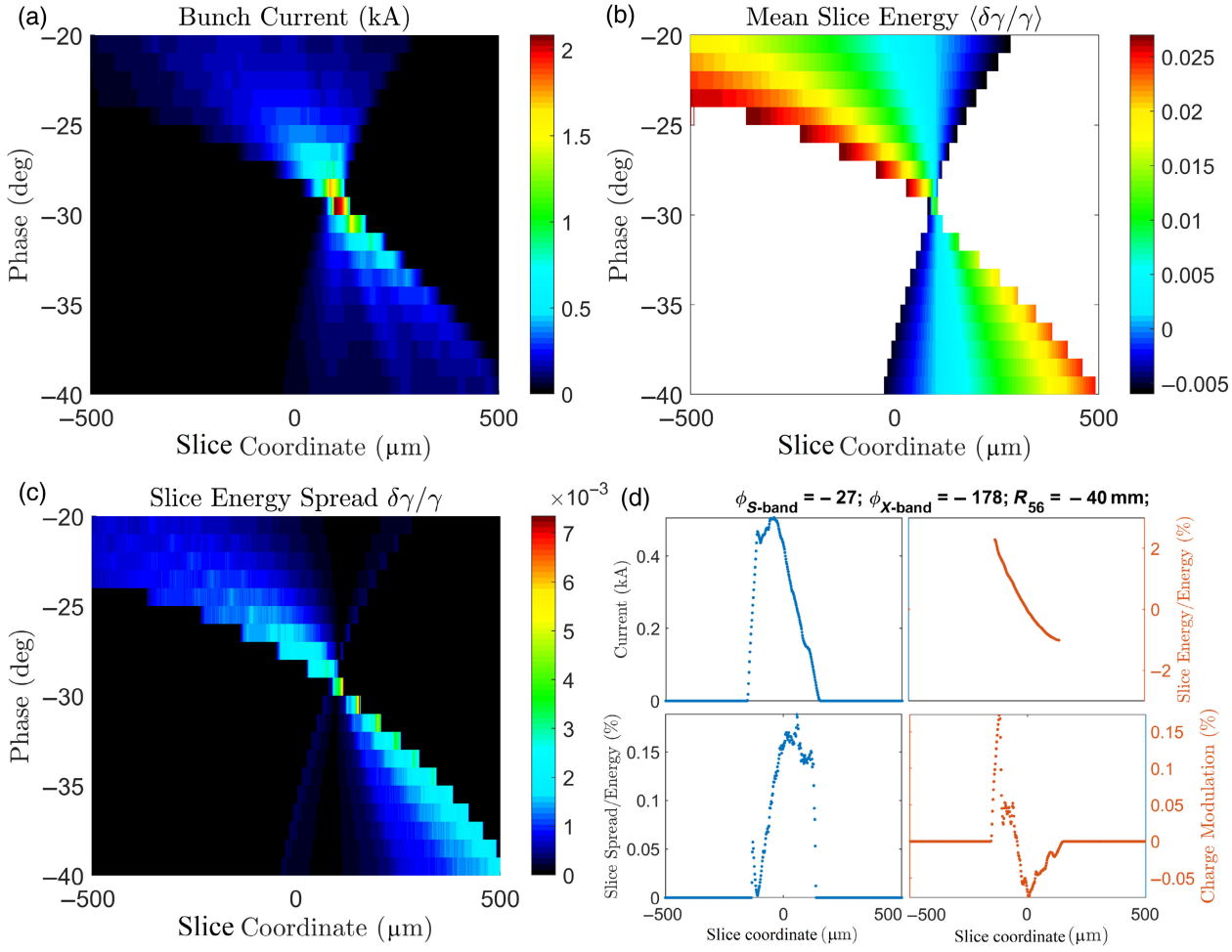



FIG. 22. LiTrack results of the phase scan of the higher-energy *S*-band injector. Plot (a): bunch current distribution; plot (b): mean slice energy along the bunch; plot (c): slice energy spread along the bunch. Plot (d): 2D distributions of the bunch current, mean slice energy and slice energy spread along the bunch; and the order-of-magnitude estimate of the energy modulation induced by the longitudinal space-charge wakefield.

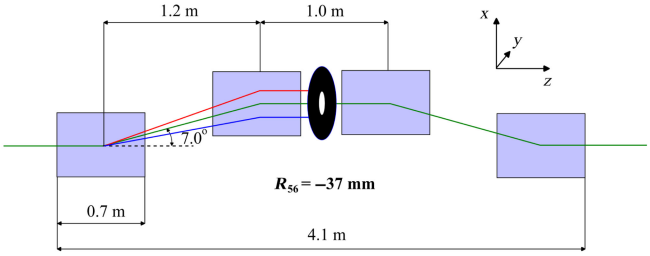



FIG. 23. Sketch of the chicane used for bunch compression in the ASTRA simulations. An aperture in the center of the chicane controls the bandwidth.

plotted in the color maps (a)–(c) of Fig. 22. The beam energy after the *S*-band linac and the *X*-band corrector are approximately 140 and 120 MeV, respectively. The phase of the *X*-band corrector is −178°. An energy filter with a bandwidth of 4% is applied to the resulting beam distribution so that the bunch charge after filtering is around 300 pC.

Thanks to the phase-space correction by means of the *X*-band cavity, the bunch can be compressed by a factor of 40 and reach a peak current of 2 kA. However, such a high peak current is unpractical for further acceleration because of the strong wakefields that it will create downstream the bunch compressor. A moderate compression by a factor of 10 is a reasonable choice, and this case is illustrated in the 2D plots of Fig. 22(d). The current distribution exhibits a plateau and the longitudinal distribution has a residual nonlinear energy-position correlation useful for further compensation of the rf curvature induced in the downstream part of the accelerator.

### B. 3D tracking with ASTRA

In order to confirm the results of the above LiTrack computations and to make sure that the beam emittance growth is acceptable, we performed 3D tracking using ASTRA. The chicane used in these simulations is depicted in Fig. 23. It includes an aperture located between the two center dipoles, which allows controlling the output bandwidth to ∼4%. In addition, the aperture permits the removal of emittance spikes associated with the energy edges of the electron bunch.

The ASTRA compression results are presented in Fig. 24 for four cases differing by the *S*-band phases; panels (e)–(h): weak compression ($\phi_{S\text{-band}} = -23°$), panels (i)–(l): mild compression ($\phi_{S\text{-band}} = -27°$), panels (m)–(p): strong compression ($\phi_{S\text{-band}} = -29.3°$), panels (q)–(t): maximum compression ($\phi_{S\text{-band}} = -30°$). The phase of the *X*-band corrector is −178°. Table III summarizes the ASTRA compression results. The first column of Fig. 24, panels (a)–(d), shows the results before the chicane. The decrease in emittances after the electron bunch has passed through the chicane, observed in Table III, is caused by the aperture,

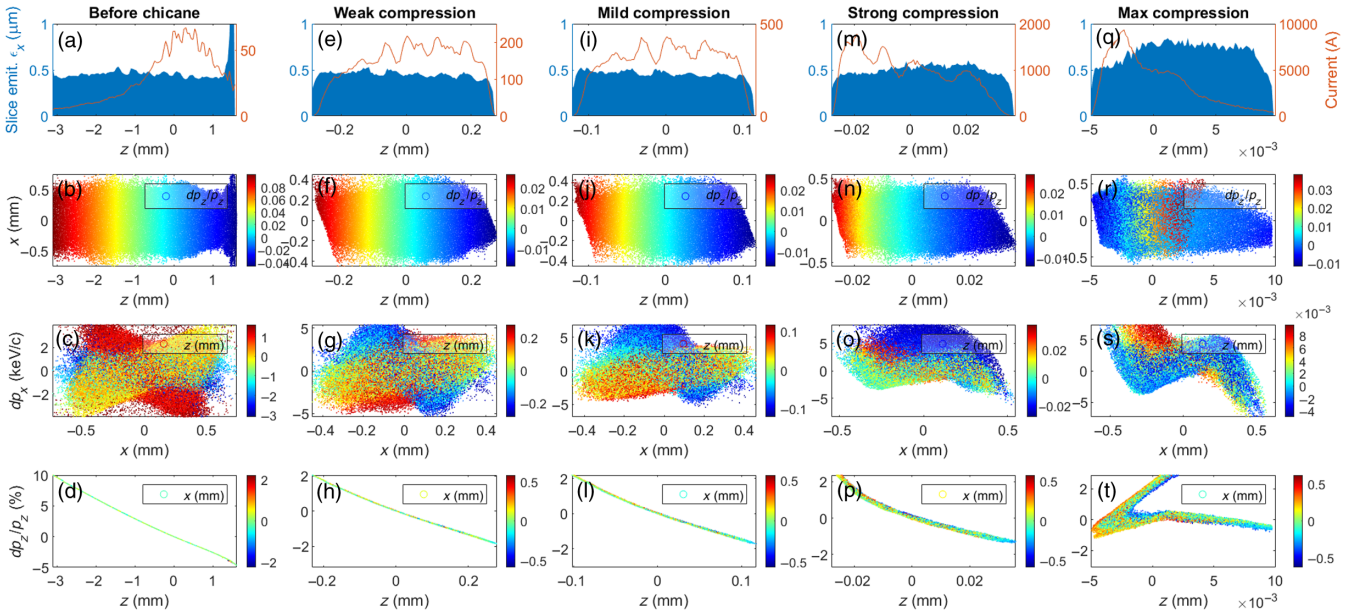



FIG. 24. ASTRA results for different bunch compressions using the chicane depicted in Fig. 23. The left column corresponds to the case before the chicane compression ($\phi_{S\text{-band}} = -27°$). Columns 2 to 5 display the increasing bunch compression accomplished by controlling the *S*-band phase; panels (e)–(h): weak compression, $\phi_{S\text{-band}} = -23°$; panels (i)–(l): mild compression, $\phi_{S\text{-band}} = -27°$; panels (m)–(P): strong compression, $\phi_{S\text{-band}} = -29.3°$; panels (q)–(t): maximum compression, $\phi_{S\text{-band}} = -30°$ The phase of the *X*-band corrector is −178°. The first row displays the bunch slice emittance in the *x* direction and current as a function of the longitudinal coordinate, the second row displays the bunch distribution in the *xz* plane, the third row displays the transverse phase space, and the fourth row displays the longitudinal phase space. The bunch distribution has been tracked all the way from the cathode to the chicane exit.

TABLE III. Summary of ASTRA-simulation results for bunch compression using the chicane depicted in Fig. 23. The four different compression cases presented are created with distinct *S*-band phases, $\phi_{S\text{-band}}$ and correspond to those in Fig. 24. The mean slice emittance is the slice emittance average weighted with the current.

| | | Compression | | | |
|---|---|---|---|---|---|
| Parameter | Before chicane | Weak | Mild | Strong | Maximum |
| $\phi_{S\text{-band}}$ | −27° | −23° | −27° | −29.3° | −30° |
| Charge (nC) | 0.50 | 0.28 | 0.24 | 0.20 | 0.18 |
| rms duration (fs) | 5150 | 461 | 194 | 54 | 11 |
| Peak current (A) | 65 | 215 | 430 | 1780 | 9350 |
| Mean slice emittance (μm) $\epsilon_x$: | 0.47 | 0.45 | 0.46 | 0.50 | 0.69 |
| $\epsilon_y$: | 0.45 | 0.46 | 0.46 | 0.46 | 0.47 |
| Projected emittance (μm) $\epsilon_x$: | 0.70 | 0.53 | 0.66 | 0.80 | 0.82 |
| $\epsilon_y$: | 0.70 | 0.49 | 0.48 | 0.47 | 0.53 |

which cuts the energy tails of the electron bunch. A slight growth of the slice- and projected x-emittances (in the chicane plane) can be observed with increasing compression of the electron bunch. The mild compression displayed in Fig. 24(i) uses the same settings of the preceding accelerating components as the LiTrack simulation shown in Fig. 22(d) and thus complements these results by adding the emittance after the chicane. The maximum compression displayed in Figs. 24(q)–24(t) reveals the potentially high peak current.

## VI. SUMMARY AND OUTLOOK

We have introduced the design and beam dynamics optimization results of a high-brightness, high-repetition-rate thermionic injector for the SACLA-II Free-Electron Laser. The proposed injector is designed to enhance the performance of SACLA by *increasing the repetition rate to the kHz level* while maintaining *low emittance and ultrashort pulse durations*. The key objective is to demonstrate that a thermionic cathode-based injector can be a competitive alternative to rf photocathode-based injectors, providing high beam quality with simpler maintenance and improved long-term stability. The simulation model describes very well the experimental situation at the SACLA gun test stand and this gives us strong confidence that the predicted performance of the new injector can be achieved in practice.

The injector concept builds upon a *500-kV pulsed dc gun with a $CeB_6$ thermionic cathode*, which has been demonstrated to produce high-brightness beams with excellent stability. To achieve femtosecond-scale bunch durations while maintaining low transverse emittance, a *multistage bunching scheme* is implemented: (i) *Ballistic bunching*: A 238-MHz rf buncher introduces a controlled energy chirp to initiate compression. (ii) *Half-wavelength bunching (HWB)*: A three-cell booster cavity provides additional compression while preserving transverse beam quality. (iii) *Velocity bunching*: The beam is further compressed in an *S*-band accelerating structure while being accelerated, reducing its longitudinal phase-space spread. (iv) *Magnetic bunching*: The longitudinal phase-space distribution is corrected in an *X*-band cavity, and the beam is finally compressed in a chicane.

A major challenge in the injector design is controlling *space-charge effects*, which can lead to emittance growth and nonlinear distortions. This is particularly critical at low energies, where space-charge forces dominate beam evolution. The study employs *3D space-charge-dominated beam tracking ASTRA simulations* to optimize beam transport through the injector.

A *genetic algorithm-based optimization* approach is applied to fine-tune injector parameters, maximizing beam brightness while minimizing emittance growth. The optimization considers (i) impact of the gun and cathode geometry; (ii) longitudinal and transverse focusing elements (rf cavities and solenoids); and (iii) hybrid magnetic lenses to mitigate aberrations and control transverse phase-space evolution.

A key finding is that the optimized injector design achieves few-hundred-picocoulomb bunches *with durations and emittances comparable to state-of-the-art C-band photocathode injectors*, demonstrating the feasibility of a thermionic-based FEL injector, see Table IV for a detailed comparison.

To ensure compatibility with the SACLA linac, the study also investigates the impact of the booster cavity design on beam transport. Two booster cavity options are analyzed: (i) *A spoke cavity design*, which provides local correction of the beam divergence by means of built-in solenoids. (ii) *A modified SPring-8 booster cavity*, offering better rf field uniformity and strong bunch compression.

Furthermore, *magnetic compression* in a higher-energy chicane is studied to assess the feasibility of further bunch length reduction. The bunch's longitudinal phase space is optimized by means of an *X*-band corrector cavity to ensure efficient compression in subsequent accelerator sections.

This study provides a solid foundation for the next-generation SACLA injector upgrade, with several key areas

TABLE IV. Comparison of injector performance for high and low charge regimes between the INFN C-band photoinjector and the SACLA thermionic injector. Values are taken directly from Table I in Ref. [22] and Table III of this work.

| Parameter | INFN high charge | This study high charge | INFN low charge | This study low charge I | This study low charge II |
|---|---|---|---|---|---|
| Charge (pC) | 500 | 500 | 200 | 240 | 200 |
| Beam energy (MeV) | 125 | 120 | 200 | 120 | 120 |
| Peak current (A) | 70 | 65 (before chicane) | 500 | 430 | 1780 |
| rms duration (fs) | 2400 | 5150 | 183 | 194 | 54 |
| Mean slice emittance (μm) | 0.44 | 0.47 | 0.45 | 0.46 | 0.48 |
| Projected emittance (μm) | 0.65 | 0.70 | 0.69 | 0.56[a] | 0.61[a] |

[a]It indicates a geometric mean value.

identified for further research and experimental validation: (i) *Experimental validation of HWB compression*: The proposed half-wavelength bunching scheme must be thoroughly tested before it can be implemented in an injector. Such a test is already being planned at the SACLA prototype test facility. (ii) *Integration with the SACLA linac*: The optimized injector must be seamlessly integrated with the existing accelerator infrastructure, ensuring compatibility with acceleration in downstream *C*-band cavities. (iii) *Exploration of alternative booster cavity geometries*: Further studies will evaluate the technical performance of the spoke cavity and SPring-8 booster cavity to ensure beam quality and energy stability, particularly for high-repetition-rate applications. (iv) *Machine learning-based injector tuning*: The implementation of real-time machine learning algorithms will allow one to automate injector tuning using genetic optimization findings, improving long-term operational performance and stability. (v) *Potential applications to low-voltage cw VHF rf and SRF guns*: The injector design principles developed in this study can be extended to continuous-wave (cw) VHF rf guns and superconducting rf guns, broadening its relevance to future FEL and ultrafast electron diffraction applications.

In conclusion, this study lays the groundwork for the development of a next-generation FEL injector capable of delivering high-brightness, high-repetition-rate electron beams. The proposed design represents a significant step forward in thermionic injector technology, offering an efficient, stable, and low-maintenance alternative to conventional rf photocathode injectors. Future work will focus on further optimizing beam quality, experimentally validating key design choices, and assessing long-term operational feasibility.

## ACKNOWLEDGMENTS

A. O. acknowledges funding through the MSCA4 Ukraine project 1232628 funded by the European Union. The present study relies extensively on beam dynamics optimization using ASTRA simulations in combination with MATLAB's built-in genetic algorithm. Dr. Kevin Pepitone developed the initial MATLAB script for automated ASTRA control, Dr. Georgii Shamuilov integrated a MATLAB-based genetic algorithm with ASTRA, and Dr. Giovanni Perosa refined and implemented the version of the MATLAB control script used in this study. Finally, we thank Dr. Tetsuya Ishikawa and Dr. Hitoshi Tanaka of RIKEN SPring-8 Center for encouraging this research as an upgrade program of the electron source and injector of SACLA.

## DATA AVAILABILITY

The data that support the findings of this article are not publicly available. The data are available from the authors upon reasonable request.

[1] P. Emma, R. Akre, J. Arthur, R. Bionta, C. Bostedt, J. Bozek, A. Brachmann, P. Bucksbaum, R. Coffee, F.-J. Decker *et al.*, Nat. Photonics **4**, 641 (2010).
[2] T. Ishikawa, H. Aoyagi, T. Asaka, Y. Asano, N. Azumi, T. Bizen, H. Ego, K. Fukami, T. Fukui, Y. Furukawa *et al.*, Nat. Photonics **6**, 540 (2012).
[3] R. Neutze, R. Wouts, D. van der Spoel, E. Weckert, and J. Hajdu, Nature (London) **406**, 752 (2000).
[4] C. Bostedt, S. Boutet, D. M. Fritz, Z. Huang, H. J. Lee, H. T. Lemke, A. Robert, W. F. Schlotter, J. J. Turner, and G. J. Williams, Rev. Mod. Phys. **88**, 015007 (2016).
[5] J. Rossbach, J. R. Schneider, and W. Wurth, Phys. Rep. **808**, 1 (2019).
[6] I. Ko, H.-S. Kang, H. Heo, C. Kim, G. Kim, C.-K. Min, H. Yang, S. Baek, H.-J. Choi, G. Mun *et al.*, Appl. Sci. **7**, 479 (2017).
[7] C. Milne, T. Schietinger, M. Aiba, A. Alarcon, J. Alex, A. Anghel, V. Arsov, C. Beard, P. Beaud, S. Bettoni *et al.*, Appl. Sci. **7**, 720 (2017).
[8] W. Decking, S. Abeghyan, P. Abramian, A. Abramsky, A. Aguirre, C. Albrecht, P. Alou, M. Altarelli, P. Altmann, K. Amyan *et al.*, Nat. Photonics **14**, 391 (2020).
[9] H. Zhang, S. Gilevich, A. Miahnahri, S. C. Alverson, A. Brachmann, J. Duris, P. Franz, A. Fry, J. Hirschman, K. Larsen *et al.*, High Power Laser Sci. Eng. **12**, e1 (2024).
[10] T. Liu, N. Huang, H. Yang, Z. Qi, K. Zhang, Z. Gao, S. Chen, C. Feng, W. Zhang, H. Luo *et al.*, Front. Phys. **11**, 1 (2023).

[11] T. Ishikawa, Photonics **9**, 357 (2022).

[12] H. Tanaka, T. Inagaki, T. Hara, and T. Ishikawa, in *Proceedings of the 14th International Particle Accelerator Conference, IPAC-2023, Venice, Italy* (JACoW, Geneva, Switzerland, 2023), Vol. 10, pp. 2590–2593, https://accelconf.web.cern.ch/ipac2023/doi/jacow-ipac2023-weoga3/.

[13] T. Shintake, H. Matsumoto, T. Ishikawa, H. Kitamura, O. Tatchyn, A. K. Freund, and T. Matsushita, in Optics for fourth-generation x-ray sources, edited by R. O. Tatchyn, A. K. Freund, and T. Matsushita, SPIE Proceedings Vol. 4500 (SPIE-International Society for Optical Engineering, Bellingham, WA, 2001), pp. 12–23, 10.1117/12.452964.

[14] K. Togawa, T. Shintake, T. Inagaki, K. Onoe, T. Tanaka, H. Baba, and H. Matsumoto, Phys. Rev. ST Accel. Beams **10**, 020703 (2007).

[15] T. Shintake, H. Tanaka, T. Hara, T. Tanaka, K. Togawa, M. Yabashi, Y. Otake, Y. Asano, T. Bizen, T. Fukui *et al.*, Nat Photonics **2**, 555 (2008).

[16] K. Togawa, Rev. Sci. Instrum. **95**, 043304 (2024).

[17] H. Tanaka, T. Watanabe, T. Abe, N. Azumi, T. Aoki, H. Dewa, T. Fujita, K. Fukami, T. Fukui, T. Hara *et al.*, J. Synchrotron Radiat. **31**, 1420 (2024).

[18] T. Asaka, H. Ego, H. Hanaki, T. Hara, T. Hasegawa, T. Hasegawa, T. Inagaki, T. Kobayashi, C. Kondo, H. Maesaka *et al.*, Phys. Rev. Accel. Beams **20**, 080702 (2017).

[19] K. Togawa, T. Hara, and H. Tanaka, Phys. Rev. ST Accel. Beams **12**, 080706 (2009).

[20] R. Akre, D. Dowell, P. Emma, J. Frisch, S. Gilevich, G. Hays, P. Hering, R. Iverson, C. Limborg-Deprey, H. Loos *et al.*, Phys. Rev. ST Accel. Beams **11**, 030703 (2008).

[21] Y. Ding, A. Brachmann, F.-J. Decker, D. Dowell, P. Emma, J. Frisch, S. Gilevich, G. Hays, P. Hering, Z. Huang *et al.*, Phys. Rev. Lett. **102**, 254801 (2009).

[22] A. Giribono, D. Alesini, F. Cardelli, G. Di Raddo, L. Faillace, M. Ferrario, A. Gallo, A. Gizzi, S. Lauciani, A. Liedl *et al.*, Phys. Rev. Accel. Beams **26**, 083402 (2023).

[23] G. D'Auria, W. Wuensch, A. Wawrzyniak, X. Janssen, D. Schulte, G. Burt, Q. Gu, T. Charles, and J. Clarke, in *Proceedings of 27th Linear Accelerator Conference, LINAC-2014, Geneva, Switzerland* (JACoW, Geneva, Switzerland 2014), MOPP023.

[24] A. Opanasenko, G. Perosa, J. Ribbing, and V. Goryashko, New J. Phys. **25**, 123049 (2023).

[25] L. Serafini, AIP Conf. Proc. **581**, 87 (2001).

[26] S. G. Anderson, P. Musumeci, J. B. Rosenzweig, W. J. Brown, R. J. England, M. Ferrario, J. S. Jacob, M. C. Thompson, G. Travish, A. M. Tremaine *et al.*, Phys. Rev. ST Accel. Beams **8**, 014401 (2005).

[27] B. Carlsten, Nucl. Instrum. Methods Phys. Res., Sect. A **285**, 313 (1989).

[28] M. Ferrario, D. Alesini, A. Bacci, M. Bellaveglia, R. Boni, M. Boscolo, M. Castellano, E. Chiadroni, A. Cianchi, L. Cultrera *et al.*, Phys. Rev. Lett. **104**, 054801 (2010).

[29] L. Serafini and J. B. Rosenzweig, Phys. Rev. E **55**, 7565 (1997).

[30] T. P. Wangler, *RF Linear Accelerators* (John Wiley & Sons, New York, 2008).

[31] H. Suzuki, T. Harami, Y. Miyahara, T. Rizawa, S. Satoh, Y. Tanabe, K. Yoshiyuki, T. Nagafuchi, S. Kawazu, and M. Nakano, in *Proceedings of the 18th Particle Accelerator Conference* (IEEE, New York, 1999), pp. 707–709.

[32] ASTRA—A space charge tracking algorithm, http://www.desy.de/~mpyflo/ (2017).

[33] J. Delayen, Nucl. Instrum. Methods Phys. Res., Sect. B **40–41**, 892 (1989).

[34] R. Garoby, A. Vergara, H. Danared, I. Alonso, E. Bargallo, B. Cheymol, C. Darve, M. Eshraqi, H. Hassanzadegan, A. Jansson *et al.*, Phys. Scr. **93**, 014001 (2017).

[35] H. Aït Abderrahim, P. Baeten, D. De Bruyn, and R. Fernandez, Energy Convers. Manage. **63**, 4 (2012).

[36] C. S. Hopper and J. R. Delayen, Phys. Rev. ST Accel. Beams **16**, 102001 (2013).

[37] K. Deitrick, G. Krafft, B. Terzić, and J. Delayen, Phys. Rev. Accel. Beams **21**, 080703 (2018).

[38] K. Floettmann, Phys. Rev. ST Accel. Beams **6**, 034202 (2003).

[39] K. Floettmann, Phys. Rev. ST Accel. Beams **18**, 120102 (2015).

[40] K. Floettmann, Phys. Rev. Accel. Beams **20**, 013401 (2017).

[41] K. Bane and P. Emma, in *Proceedings of the 21st Particle Accelerator Conference, Knoxville, TN, 2005* (IEEE, Piscataway, NJ, 2005), pp. 4266–4268, 10.1109/PAC.2005.1591786.